Optimization and Control of Burning Plasmas Through High Performance Computing

DOE Grant DE-SC0012174

Technical Final Report

Performance period: June 1, 2014 – May 31, 2017

A.Y. Pankin

Tech-X Corporation, Boulder, CO, USA

Current affiliation: Lawrence Livermore National Laboratory, Livermore, CA, USA

Progress in the following research categories has been made. These categories are:

- **Task 1:** Understanding of anomalous transport in the H-mode pedestal region of Alcator C-Mod tokamak[1–4];
- **Task 2:** Investigation of high beta poloidal DIII-D discharges[5–11];
- **Task 3:** Investigation of the plasma shaping effects on the H-mode pedestal structure using coupled kinetic neoclassical/MHD stability simulations[12];
- **Task 4:** Modeling of poloidal rotation profiles in the plasma core of the DIII-D tokamak;
- **Task 5:** Investigating the effects of the pedestal height and width on the plasma confinement in ITER;
- **Task 6:** Core-edge modeling and the investigation of heat fluxes on divertor plates[13];
- **Task 7:** Investigation of particle transport in tokamaks[14,15];
- **Task 8:** Advancing the uncertainty quantification methods for the integrated modeling codes[16–19];
- **Task 9:** Development of reduced modules for anomalous transport[20–24];
- **Task 10:** Predictive modeling of operational scenarios in ITER[25–27];
- **Task 11:** Development and maintenance of the FACETS physics components, tools and utilities[28];
- **Task 12:** Updating the equilibrium interfaces in the FACETS code;
- **Task 13:** Collaboration with IPP (China) and JAEA (Japan) scientists on predictive modeling of tokamak scenarios in EAST and JT60-U.

This project has revived the FACETS code, that has been developed under SciDAC funding in 2008-2012. The code has been dormant for a number of years after the SciDAC funding stopped. FACETS depends on external packages. The external packages and libraries such as PETSc, FFTW, HDF5 and NETCDF that are included in FACETS have evolved during these years. Some packages in FACETS are also parts of other codes such as PlasmaState, NUBEAM, GACODES, and UEDGE. These packages have been also evolved together with their host codes which include TRANSP, TGYRO and XPTOR. Finally, there is also a set of packages in FACETS that are being developed and maintained by Tech-X. These packages include BILDER, SciMake, and FcioWrappers. Many of these packages evolved significantly during the last several years and FACETS had to be updated to synchronize with the recent progress in the external packages. The PI has introduced new changes to the BILDER package to support the updated interfaces to the external modules. During the last year of the project, the FACETS version of the UEDGE code has been extracted from FACETS as a standalone package[28]. The PI collaborates with the scientists from LLNL on the updated UEDGE model in FACETS. Drs. T. Rognlien, M. Umansky and A. Dimits from LLNL are contributing to this task.

Several physics related tasks in which the PI is a leading contributor and where the significant progress is archived are described in more details below.

I. STUDY OF ANOMALOUS TRANSPORT IN THE PLASMA EDGE OF ALCATOR C-MOD TOKAMAK

Tokamak edge physics plays a key role in controlling the global plasma confinement of tokamak discharges since the edge region sets the boundary conditions for the whole discharge. In particular, the transition from the low plasma confinement mode (L-mode) to enhanced plasma confinement mode (H-mode) is associated with the formation of an edge transport barrier or H-mode pedestal. It is commonly accepted that the H-mode pedestal height is defined by the stability conditions of peeling and ballooning modes, which limit the accumulation of free energy in the pedestal. It is also believed that the H-mode pedestal slope is determined by the level of thermal, particle and momentum transport in the pedestal. While the nature of neoclassical transport is well established, the driving mechanisms of turbulence which result in anomalous transport in the plasma edge region are still being discussed. Understanding edge anomalous transport and the mechanisms that result in suppression is important for the development of a comprehensive model for the H-mode pedestal.

A large number of models for anomalous transport has been developed during the last several decades. For the model described in Ref.[29], the anomalous transport in the pedestal is driven by drift-wave turbulence which is significantly suppressed by the $\mathbf{E}\times\mathbf{B}$ flow shear. The idea of pedestal anomalous transport driven by ideal ballooning modes suppressed by the diamagnetic effects is explored in Ref.[30]. An alternative approach to the pedestal transport driven through the paleoclassical mechanism is investigated in Refs.[31–33]. Several models of anomalous transport that define the H-mode pedestal slope are compared in Ref.[34].

Many drift-wave instabilities drive the anomalous transport which is very stiff. As a result of the transport stiffness, the plasma gradients in the H-mode region remain close to the linear stability boundary of the most unstable modes that drive the anomalous transport. The pedestal slope in these models can be obtained from the analysis of the stability conditions of the most unstable modes. This approach is used in the EPED model[35] that postulates that the main modes that drive the pedestal transport are kinetic ballooning modes (KBMs) and that the pedestal slope is defined by the linear stability of these modes. The KBMs are electromagnetic modes that are destabilized above critical value of β^{crit}. Similar to the

ITG modes, the stability of KBM modes are dependent on the parameter η_i that is defined as a ratio of temperature and density gradients. The EPED model has been verified for a number of tokamaks and good agreement between experimental data and model prediction has been reported for Alcator C-Mod, DIII-D, and NSTX discharges.[36].

In spite the success of the EPED model, the questions remain whether the KBMs are the dominant pedestal modes in all plasma regimes and what is the confidence level for using this model for future tokamaks and for new plasma regimes. For example, if is not clear what modes drive the anomalous transport in low β plasmas where the KBMs are expected to be stable and in highly collisional plasmas where the most drift-wave instabilities are expected to significantly damped by collisions. In this study, drift resistive ballooning inertial modes (DRIBMs)[37] are examined to determine if they can also play a role in the setting of the H-mode pedestal slope. The DRIBMs can result in the turbulence that drives the anomalous transport in the edge region of tokamaks[30,38]. These modes can explain some experimental observation such as a strong poloidal asymmetry in poloidal particle transport[39]. It has also been demonstrated previously that the DRIBMs can play a significant role at the plasma edge of Ohmic and L-mode discharges[23]. The differences in the destabilization mechanisms of KBMs and DRIBMs can be used to distinguish these modes in the analysis of experimental data.

In this study, the integrated modeling codes are used to investigate the possible role of the DRIBMs in the plasma edge region of five Alcator C-Mod discharges that represent a plasma density scan. The DRIBM model, based on the reduced Braginski equations, is implemented as a component of the Multi-Mode Model for anomalous transport[40] and is used in the analysis presented in this report. In addition, the kinetic neoclassical XGC0 code[41] is used to investigate the scaling of anomalous transport in the H-mode pedestal region with respect to plasma collisionality. In order to investigate the dependence of anomalous transport on plasma collisionality, the additive flux minimization technique[33], based on uncertainty quantification analysis, is used.

Five Alcator C-Mod discharges that represent the plasma density scan are analyzed in this report. These discharges are 1120815010, 1120815014, 1120815020, 1120815023 and 1120815027. The line average density is varied in the range from $1.6\times10^{20}\ m^{-3}$ to $2.7\times10^{20}\ m^{-3}$. Comparing the H-mode pedestal regions, one can notice that the Alcator C-Mod discharges 1120815010 and 1120815014 have largest plasma and pedestal densities, the Alcator C-Mod discharge 1120815027 has an intermediate plasma and pedestal density, and the Alcator C-Mod discharges 1120815020 and 1120815023 have the lowest plasma and pedestal densities and highest plasma temperatures at the diagnostic times chosen. The five Alcator C-Mod discharges studied have similar plasma current $I_\mathrm{p} \approx 0.9MA$ during the discharge period considered and similar current profiles. As result of similar current profiles, the discharges have also similar q-profiles which are found during EFIT equilibrium reconstruction. The q-profiles have the almost the same q_{95}, but they somewhat diverge in the outer region of the H-mode pedestals. The drift resistive ballooning modes are sensitive to the q-profiles and the differences outside of $\rho = 0.95$ can affect the comparison. In our linear stability analysis studies described below, we limit our comparison to the region from $\rho = 0.90$ to $\rho = 0.95$, which corresponds to the region where the top of the pedestal is located in these discharges.

The plasma collisionality and neoclassical resistivity depend on the temperatures and densities and vary significantly in the Alcator C-Mod discharges studied. The resistivity and collisionality are important factors affecting the DRIBMs and both have a destabilizing

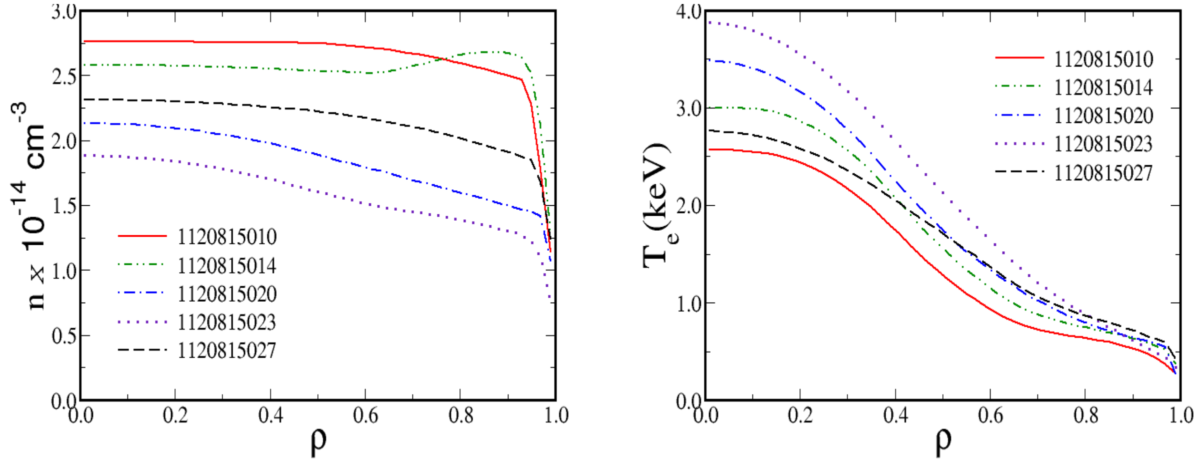

FIG. 1. The electron density (left) and electron temperature (right) profiles versus square root of normalized toroidal flux for five Alcator C-Mod discharges studied.

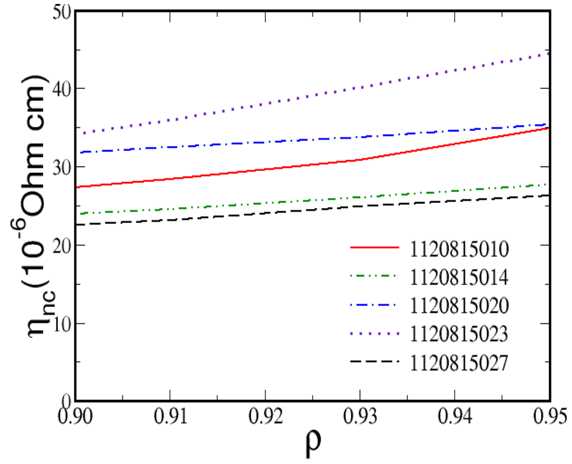

FIG. 2. The neoclassical resistivity profiles versus square root of normalized toroidal flux for five Alcator C-Mod discharges studied.

effect on the modes. The neoclassical resistivity profiles for the plasma edge regions are given in Fig. 2 and the electron and ion collisionalities are given in Fig. 3.

A. Linear Stability Analysis of DRIBMs

The anomalous transport driven by the DRIBMs can be described using the DRIBM model[37] which is a part of the Multi-Mode transport model[40]. The DRIBM model is based on fluid description and utilizes the reduced Braginski equations. The model consists of six linearized equations including the ion continuity equation, the equations for vorticity, electron and ion energies, and total momentum, as well as the generalized Ohm's law. The equations take into account the diamagnetic effects, parallel electron and ion dynamics, electron inertia, magnetic perturbations, and gyro-viscous stress terms. The electron trapping,

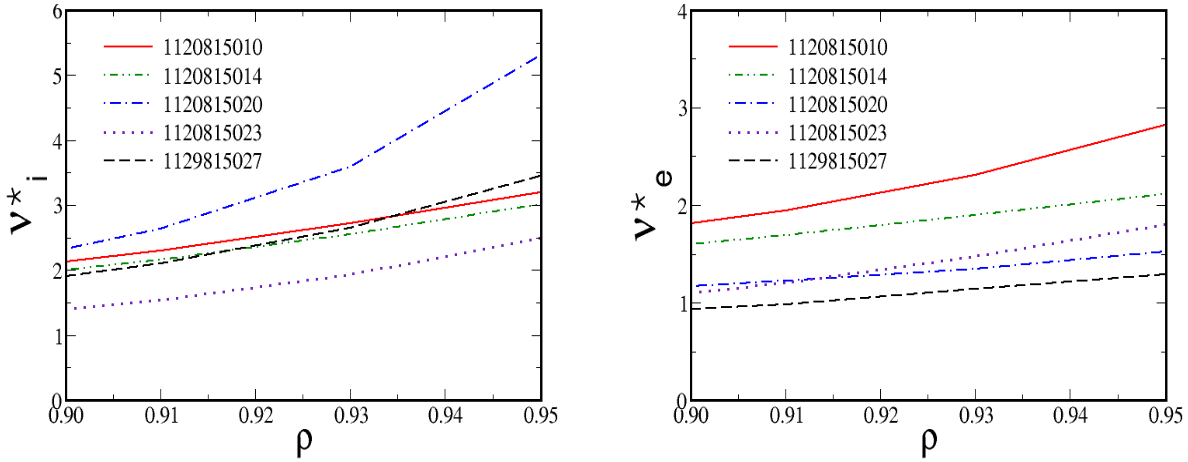

FIG. 3. Ion (left) and electron (right) collisionality versus square root of normalized toroidal flux for five Alcator C-Mod discharges studied.

displacement currents and effects of impurity ions are neglected in the model. The DRIBM model solves the differential equations which are integrated as an initial value problem with guesses for unknown initial values[22] in order to compute the growth rates and frequencies.

The DRIBMs are destabilized by the current density, density gradients, collisionality and resistivity. The modes are stabilized by the temperature gradients. Typical dependence of the DRIBM effective diffusivities on collision frequency are shown in Fig. 4. The DRIBMs differ from the KBMs which can be destabilized by density and temperature gradients, stabilized by collisionality, and which are independent of resistivity.

The growth rates and frequencies computed using the DRIBM model are plotted in Fig. 5 as a function of the normalized radius. The DRIBMs are found to be unstable in the region near the top of the pedestal for all five Alcator C-Mod discharges. However, the growth rates for the Alcator C-Mod discharge 1120815020 remains marginally small through the whole plasma edge region analyzed in this study. The DRIBMs are found to be the most unstable for the Alcator C-Mod discharges 1120815010 and 1120815014 which have the largest pedestal densities and are among the discharges with the smallest pedestal temperatures. These two discharges also have the largest electron collisionalities. The ion collisionalities for these two discharges in the middle range and the neoclassical resistivities are below average. While all collisionalities as well as neoclassical resistivity remain the destabilizing factors for the DRIBMs, the electron collisionality is found to be the strongest destabilizing factor for the DRIBMs in the Alcator C-Mod discharges.

The dependence on the plasma collisionality distinguishes the DRIBMs from many drift-wave instabilities that are damped by the plasma collisions. While the stability analysis of other modes that can drive the anomalous transport in the H-mode pedestal is outside the scope of this report, one can easily envision the situation when the DRIBMs are strongly destabilized and all other potential contributors to the H-mode pedestal structure are stabilized in highly collisional plasmas. It is likely that the DRIBMs need to be considered along with other modes when developing a model for the H-mode pedestal slope in highly collisional plasmas with relatively low pedestal temperatures.

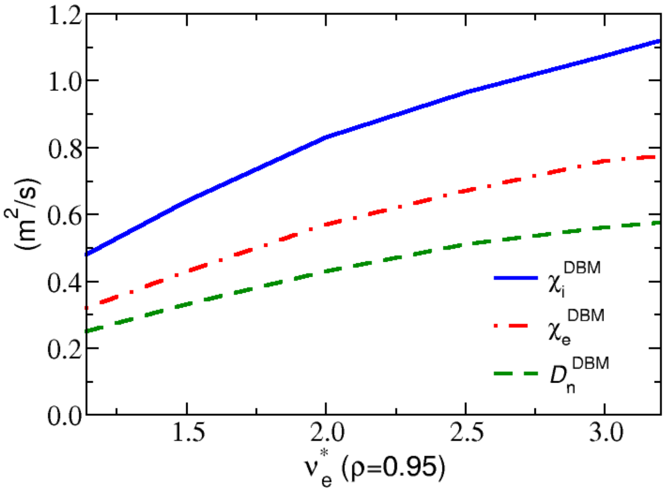

FIG. 4. The effective particle and thermal diffusivities as a function of plasma collision frequency computed using the DRIBM model for the DIII-D geometry.

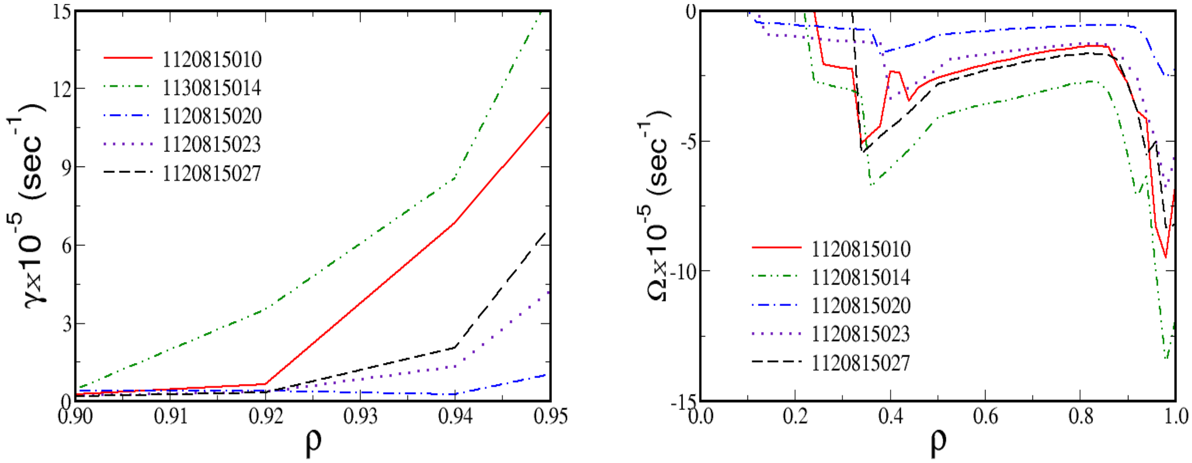

FIG. 5. The growth rates (left) and frequencies (right) versus square root of normalized toroidal flux for five Alcator C-Mod discharges studied.

B. Collisionality Scaling of Anomalous Transport in the H-Mode Pedestal

An alternative approach for testing the role of the DRIBMs in the plasma edge region is to verify that the anomalous transport follows a particular scaling characteristic associated with these modes. Such a test is not linked to any particular model for the DRIBMs. The dependence on the plasma collisionality distinguishes the DRIBMs from many other modes that can drive the anomalous transport in the plasma edge. If the dominant instabilities that drive the edge anomalous transport are the DRIBMs, the dependence of the effective diffusivity on the collisionality will look similar to the dependence shown in Fig. 4.

For the analysis of the anomalous transport dependence on the collisionality, the additive flux minimization technique (AFMT)[33] is used together with the kinetic neoclassical XGC0 code[41]. The XGC0 code computes the neoclassical transport at high fidelity, but utilizes a simplified model for anomalous transport[13]. The electron thermal, ion thermal, and particle effective diffusivities are free parameters in the code that can be specified in the XGC0 input files. Using AFMT, one can use these effective diffusivities as parameters in the optimization task on minimizing the differences between plasma profiles predicted with the XGC0 code and the corresponding experimental plasma profiles.

For stiff-transport models which are sensitive to fluxes, the key AFMT concept is to add an additional time-varying flux that then becomes an unknown to be optimized so as to maintain the profiles near the experimental profiles. Specifically, for our analysis, the most general unknown vector is $\vec{x} = (n_s, E_s)$, where s ranges over all of the species within the plasma; n_s and E_s are the density and energy of plasma specie s. Defining $\vec{x}_{predict}$ and $\vec{x}_{exp}$ as the state variables that come from the simulation and experiment, respectively, one can separate the fluxes for the system into those that are predictive, based on high-fidelity validated simulations, and those that are interpretive:

$$\Gamma_x = \Gamma_{interp}(\rho, \vec{x}) + \Gamma_{predict}(\rho, \vec{x}). \tag{1}$$

Here, the predictive flux is the neoclassical flux computed using the XGC0 code and the interpretive flux is the anomalous flux. With this definition, one can choose an optimization metric and cast the problem as an optimization problem to minimize the integrated difference between the predicted and experimental values, $M = \| \vec{x}_{exp} - \vec{x}_{predict} \|$ (L_2 norm)[42]. In this research, the DAKOTA toolkit for uncertainty quantification, sensitivity analysis and optimization[43] is used to minimize the rms deviations between the computed and experimental temperature and density profiles. The gradient-based unconstrained optimization in DAKOTA is used.

The anomalous transport coefficients are adjusted in the way that the plasma profiles predicted with the XGC0 code do not significantly differ from the experimental values. The left panel in Fig. 6 shows the time dependence of the electron temperature profile for Alcator C-Mod discharge 1120815010 as a function of normalized square root of poloidal flux using the XGC0 code. The profiles nearly do not evolve from the initial profile which is set equal to the experimental profile. A similar approach has been applied to ion temperature and particle density profiles. In this report, the electron thermal diffusivities at the top of the H-mode pedestal are compared. The combined results for five Alcator C-Mod discharges are shown in the right panel of Fig. 6. While there is a significant scatter in the elecron thermal diffusivities as a function of the electron collisionality, there is a trend that the electron thermal diffusivity at the top of the pedestal increases with the electron collisionality. This trend is in an agreement with the expected dependence on the plasma collisionality for the DRIBMs. These results indicate the potential importance of the DRIBMs in highly collisional plasma discharges.

C. Summary of Anomalous Transport Studies in the Plasma Edge Region of Alcator C-Mod discharges

A possible role of the DRIBMs in the plasma edge region of five Alcator C-Mod discharges that represent the plasma density scan is investigated in this report. Two alternative methods are used to illustrate the role of the DRIBMs. The first method is based on the stability analysis of the Alcator C-Mod equilibria using the DRIBM model[37]. The second method is based on the interpretive analysis of anomalous transport in the five Alcator C-Mod discharges using the additive flux minimization technique[33]. It is demonstrated using the

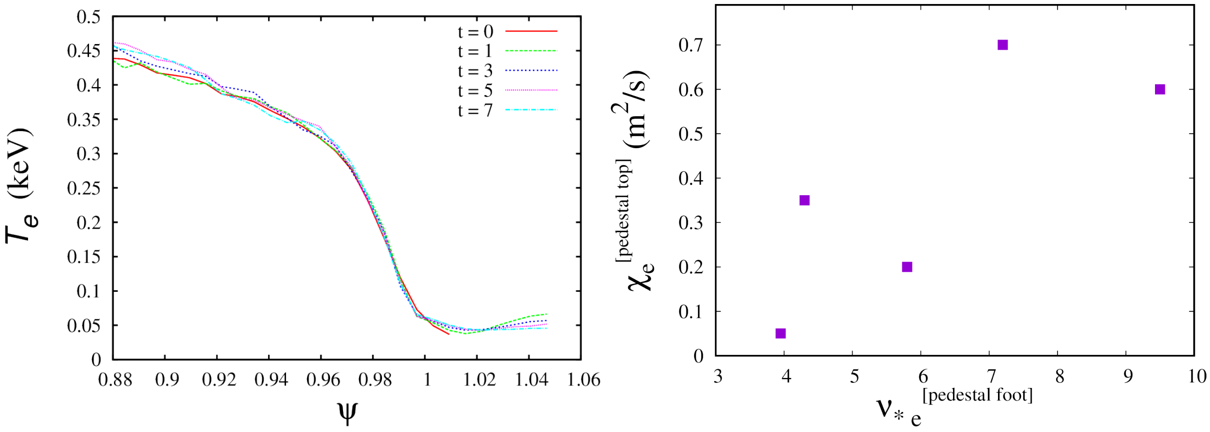

FIG. 6. Left panel shows the electron temperature profiles predicted for the Alcator C-Mod discharge 1120815010 using the XGC0 code as functions of the normalized poloidal flux. The initial experimental profile is shown as a solid curve. Other profiles are predicted using XGC0 at times t normalized to the ion transit time. Using AFMT, the interpretive anomalous transport coefficients adjusted so that the density and other profiles do not evolve in time. Right panel shows the electron thermal diffusivities at the top the H-mode pedestal for five Alcator C-Mod discharges as a function of electron collisionality computed at the bottom of the H-mode pedestal.

first method that the DRIBMs become more unstable in the discharges with larger electron collisionality. It is shown using the second method that the anomalous electron thermal transport at the pedestal top increases with the electron collisionality. There is a significant scatter in the results which is likely to be associated with the interpretation of experimental data that have relatively large error bars in the plasma edge region. The scatter might be also related to the fact that the analyzed discharges do not represent a "pure" plasma collisionality scan and the density and temperature gradients at the pedestal top change from one discharge to the other. The conclusions about the collisionality dependence of the anomalous transport can be confirmed by extending this analysis to larger number of discharges so that the statistics of analysis will improve. This consideration indicates a possible future direction of this research. However, even now one can conclude that the collisionality dependence of the plasma edge anomalous transport is in agreement with the previous experimental results from Alcator C-Mod[44,45]. However, it should be noted that these experimental observations pertain primarily to the L-mode discharges. This dependence of anomalous transport on collisionality points to the DRIBMs as one of possible instabilities that drive anomalous transport at the plasma edge in the discharges with high electron collisionality. An additional test regarding the role of these modes in other plasma parameter regimes might be achieved by extending the models for the H-mode pedestal with the linear stability condition of the DRIBMs.

The results of this research have been presented at the TTF meeting[1], H-mode workshop[2], and the APS DPPP meeting[3]. The results are also submitted for publication to Nuclear Fusion[4].

II. INVESTIGATION OF THE PLASMA SHAPING EFFECTS ON THE H-MODE PEDESTAL STRUCTURE USING COUPLED KINETIC NEOCLASSICAL/MHD STABILITY SIMULATIONS

In this study, the XGC0 code[41], which employs a neoclassical model, is combined with the ELITE (Edge Localized Instabilities in Tokamak Equilibria) code, which applies the peeling-ballooning stability conditions used in the EPED model, in order to study the H-mode pedestal dependence with the plasma elongation and triangularity. Previously, these two codes were combined in an investigation of ELM crash dynamics[46]. Neoclassical models and models that are based on the MHD constrains, such as EPED[35], can independently reproduce many experimentally observed features of the H-mode pedestal. In the EPED model, the pedestal height is limited by the stability conditions of the peeling and ballooning modes and the pedestal slope is controlled by the kinetic ballooning modes. During the H-mode pedestal recovery after an ELM crash, both the pedestal width and height increase following the constraint from the kinetic ballooning model. The slope of the H-mode pedestal typically evolve slowly according to the changes in the kinetic ballooning stability conditions. The pedestal width and height continue to grow until the peeling-ballooning instability condition is satisfied and next ELM crash occurs. The model provides good agreement with the experimental data from a number of tokamaks[36]. However, the EPED model alone does not provide the details of the pedestal buildup dynamics nor does it distinguish among the widths of the electron temperature, ion temperature and plasma density pedestals. In experiments, these widths are usually different. In particular, the ion temperature pedestal width is often significantly wider than the electron temperature and plasma density pedestal widths[47]. The EPED model is capable of taking into account the different widths observed in experiments but does not predict the separation in the pedestal width. There is also the question of how to take into account the effects of plasma collisionality in the pedestal model and if existing pedestal models can be used for discharges with very low beta where the kinetic ballooning modes are expected to be stable[4].

Effects of plasma shaping are included in the XGC0 model and in the peeling-ballooning stability conditions computed with the ELITE code[48]. While the elongation and triangularity effects can be investigated with either model, it is useful to understand the effects that comes from the interaction of neoclassical and MHD stability physics. In the studies described in this repost, the anomalous transport is intentionally reduced to a negligibly small level and the kinetic ballooning constraint is not considered. In the coupled XGC0/ELITE simulations, the height of the pedestal is determined by the peeling-ballooning stability conditions and the pedestal slope is determined by the neoclassical physics. The anomalous transport is usually strongly reduced in the H-mode pedestal region as a consequence of the strong quenching effect resulting from $\mathbf{E} \times \mathbf{B}$ flow shear. However, anomalous transport is still expected to play an important role in the H-mode pedestal buildup. In this report, the effects that can not be robustly described by the XGC0 and ELITE codes are excluded. These effects include the edge kinetic turbulence physics, core turbulence and extended MHD physics, details of impurity transport, sputtering, energetic particle influx from core and 3D magnetic field effects.

Studies are carried out to illustrate the dependence of H-mode pedestals, in tokamaks that have type I ELMs, on plasma elongation and triangularity. The objective of this study is to obtain the dependence of pedestal width and height on plasma shaping that can be tested in experiments. Three DIII-D discharges that represent a scan with respect to plasma shaping are considered: A discharge with high elongation and low triangularity, a discharge with low elongation and low triangularity, and a discharge with low elongation and high triangularity. Dependence of the pedestal width and height is developed as a function of the scanned plasma parameters. The effect of neutral temperature on the pedestal width and height is examined. Differences in the dependence of the widths of electron temperature and ion temperature pedestals are investigated.

Experimental data from three DIII-D H-mode discharges[49] that represent a scan with respect to plasma shaping are considered. The values of elongation, κ, triangularity, δ, major radius, R, minor radius, a, magnetic field strength at the axis, B_0, plasma current, $I_{\rm p}$, safety factor at the edge, $q_{\rm edge}$, and total plasma energy, $W_{\rm tot}$, are shown in Table I.

The discharge 136674 is the highly elongated discharge ($\kappa = 1.71$) which is typical for most DIII-D discharges, but with rather low triangularity ($\delta = 0.12$). The discharge 136693 has nearly circular geometry ($\kappa = 1.25$) with triangularity almost zero ($\delta = 0.03$). The discharge 136705 is also nearly circular ($\kappa = 1.26$) but has the highest triangularity ($\delta = 0.30$) among the three discharges. The discharges 136674 and 136693 correspond to the part of experimental plasma elongation campaign in which elongation is varied by almost 50%. While the discharges 136693 and 136705 correspond to the part of experimental plasma triangularity campaign in which triangularity is varied by a factor of 10. The flux surfaces computed using the equilibrium reconstruction for these three DIII-D discharges are shown in Fig. 7.

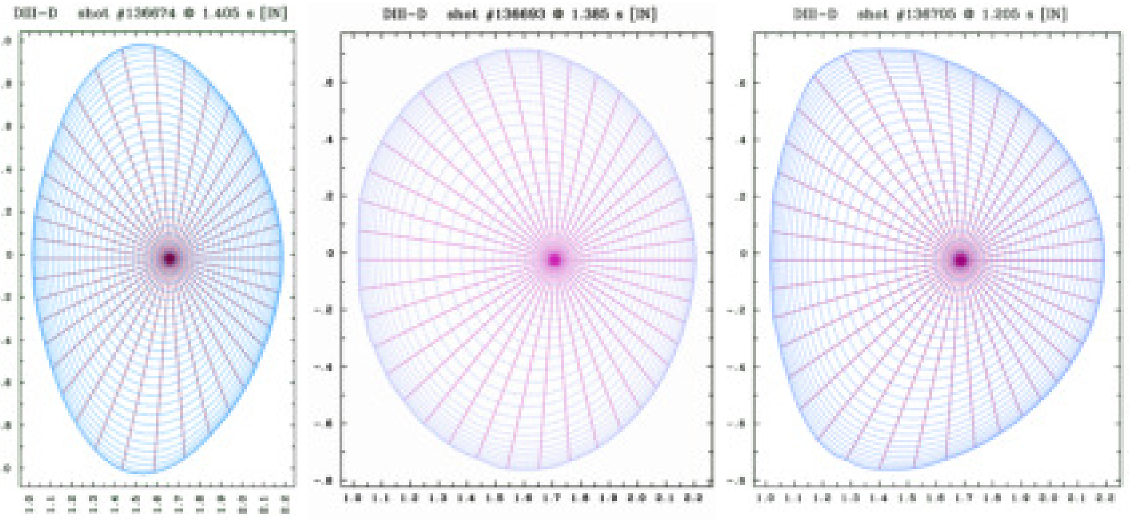

FIG. 7. (Color online) Contours of equilibrium flux surfaces with different plasma elongation and triangularity are shown in (R,Z) plane for DIII-D discharges 136674 at time t = 1.405 sec (left panel), 136693 at time t=1.385 sec (middle panel), and 136705 at time t = 1.205 sec (left panel).

The energy confinement time increases from 50 ms in the low κ case to 80 ms in the high κ case[49]. It is found that twice the heating power (two neutral beam sources) was required in the low κ case to maintain profiles similar to those obtained with a single neutral beam source in the high κ case. Also, note that there is a substantial change in the plasma current I_p. This change is necessary in order to maintain consistency in the safety factor.

The XGC0 simulations do not include the effects associated with the anomalous transport. However, the anomalous transport is taken to be a small residual level through the whole edge region for all three DIII-D discharges that are investigated in this study. The

TABLE I. The DIII-D discharges analyzed in this study and their plasma parameters.

Tokamak	DIII-D	DIII-D	DIII-D
Discharge	136674	136693	136705
Type	High Elongation	Low Elongation	High triangularity
time, sec	1.41	1.39	1.21
κ	1.71	1.25	1.26
δ	0.12	0.03	0.30
R (m)	1.70	1.70	1.70
a (m)	0.59	0.59	0.59
B_0 (T)	2.00	2.00	2.00
I_p (MA)	1.20	0.88	0.94
q_edge	5.65	4.27	5.56
W_tot (MJ)	2.56	2.52	4.31

anomalous electron and ion thermal diffusivity is set equal to 0.02 m^2/sec in the pedestal region and 0.4 m^2/sec in the SOL region and the anomalous particle diffusivity is set equal to $0.01\,m^2/sec$ in the pedestal region and $0.05\,m^2/sec$ in the scrape-of-layer region. The motivation of the selection of anomalous transport coefficients at a small residual level is that the focus of this study is the neoclassical and MHD effects on the development of the H-mode pedestal structure. However, a residual anomalous transport is still required in these simulations. In the absence of the anomalous transport, the plasma density becomes too low in the near outer separatrix region. The plasma density depletion leads to unrealistic ion and electron temperature profiles. These changes to the plasma profiles might occur before the H-mode pedestal develops enough to trigger the peeling or ballooning instabilities that would lead to an ELM crash. Without a rigorous model for anomalous transport, there is no mechanism to correctly describe the transport in the plasma edge as well the transport from the plasma core, where the neutral beam injection is mostly applied. It is not expected that the plasma profiles predicted from the coupled XGC0/ELITE simulations reproduce the experimental results. The objective of this study is to utilize in the XGC0 code the magnetic equilibria that correspond to different DIII-D plasma shapings in order to derive a scaling for the pedestal width and height from the coupled kinetic neoclassical/MHD stability simulations with respect to the plasma elongation and triangularity.

In order to compare the differences in the H-mode pedestal widths for the DIII-D discharges with different plasma shaping, the plasma density and electron temperature profiles are normalized to bring them to the same scale. In Fig. 9, the normalized plasma density and normalized temperature profiles for all three DIII-D discharges with different elongations and triangularities are presented. It is found that the pedestal width for the plasma density profiles is the smallest for the high elongation discharge, 136674, and the pedestal width for the electron density profile is the smallest for the high triangularity discharge, 136693. The pedestal width for the plasma density profiles is found to be decreasing with increasing elongation (compare a curve indicating 136674 with 136693 and 136705 curves) and is almost independent of triangularity (compare a curve indicating 136693 with a curve indicating 136705). In the discharges considered in this study, the effect of increased elongation manifests itself in the plasma density profiles first, while the effect of increased triangularity manifests itself in the electron temperature profiles first. The pedestal height is found to be significantly larger in the discharges with larger elongation. It has also been found that the pedestal width for the electron temperature profiles is found to be almost independent of elongation and show a weak dependence on the triangularity. The pedestal width for ion temperature profiles is found to be much wider than the pedestal width for the plasma density and electron temperature profiles (not shown here). Neoclassical effects together with the MHD stability conditions that are verified using the ideal stability ELITE code can explain some experimental trends such as the dependence of the ELM frequency on the plasma elongation[50] and the dependence of the H-mode pedestal height on triangularity[51]. The question about the contributions of the anomalous transport in the pedestal and SOL regions remains. The role of anomalous transport will be addressed in future studies.

The neoclassical effects are combined with the peeling-ballooning stability conditions in order to study the dependence of H-modes pedestal on plasma elongation and triangularity. The anomalous thermal and particle transport is included at a small residual level in the H-mode pedestal region. The growth of the pedestal is limited by an ELM instability criterion computed using the ELITE MHD stability code. The kinetic neoclassical XGC0 code and ELITE ideal MHD stability code coupling is automated in the EFFIS computer science framework. Three DIII-D ELMy H-mode discharges with high elongation and low triangularity, with low elongation and low triangularity, and with low elongation and high triangularity are considered. It is found that the H-mode pedestal in simulations continues to grow and pedestal width continues to decrease in the absence of MHD stability constraints. MHD constrains do not affect the dynamics of an ELM crash. They set the final time, beyond which the plasma profiles become MHD unstable and can not be reached in the experiments. At the time of an ELM crash, the slope of the H-mode pedestal reaches a semi-steady state and evolves slowly for higher elongation and higher triangularity geometry. The dynamics of maximum bootstrap current densities as function of maximum pressure gradients for all three discharges are shown in Fig. 8. The arrows show the direction of time and large dots mark the conditions that would lead to an ELM crash. The ELM crashes in the discharges with weak shaping occur at lower plasma bootstrap current densities and lower plasma pressure gradients. This is consistent with a reduced stable region for the discharges with weak shaping (for example, see Fig. 2b in Ref[52]). For lower elongation and lower triangularity, the plasma profiles in the H-mode pedestal evolve rapidly at the time of crash. The ELM frequency is the largest and the H-mode pedestal height is the smallest for the discharge with the low elongation and low triangularity. The ELM frequency is the smallest and the pedestal height is the largest for the high elongation discharge. The discharge with low elongation and high triangularity has an average ELM frequency and H-mode pedestal height. The effect of neutral temperature on the pedestal width and height is found to be weak. However, the peeling-ballooning mode becomes unstable earlier in the ion transit periods with increasing neutral temperature.

The elongation and triangularity affect the pedestal density differently than they effect the pedestal temperature. The width of the pedestal density is found to decrease with increasing elongation and is almost independent of triangularity. The effect of increased elongation manifests itself in the plasma density profiles first, while the effect of increased

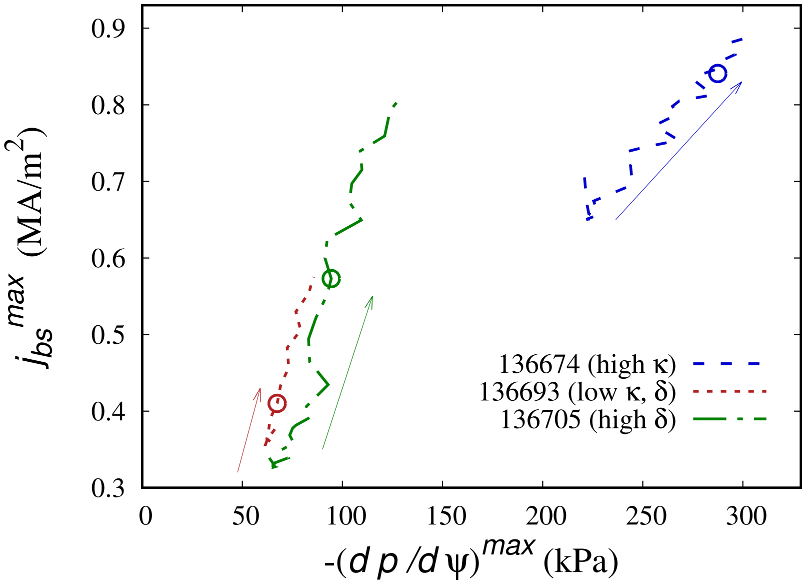

FIG. 8. (Color online) The time histories of maximum bootstrap current densities as functions of maximum pressure gradients in the H-mode pedestal region for three DIII-D discharges with different elongations and triangularities. The arrows show the direction of time and large dots indicate the conditions for triggering of ELM crashes.

triangularity manifests itself in the electron temperature profiles first.

The anomalous transport included in this study is at a small residual level and is independent of the plasma parameters. In order to investigate the role of the anomalous transport on the H-mode pedestal buildup in the tokamak discharges with different plasma shaping, coupled gyro-kinetic XGC1/MHD stability simulations will be considered in future. It should be also noted that the experimental equilibria have been used to investigate the dependencies of the pedestal width and height on the elongation and triangularity. In the experimental equilibria, there are factors other than elongation and triangularity that can affect the pedestal width and height. In particular, the plasma currents in the high and low elongation discharges in this research differ by approximately 25%. There also differences in q-profiles. In the EPED model, the differences in plasma currents can explain larger pedestal gradients for the discharge with the larger elongation. The plasma current might have a strong effect on the pedestal width and height[53]. While it is expected that the neoclassical XGC0 code captures many effects associated with the differences in the plasma currents[13], it is difficult to separate if the changes in the predicted pedestal width and height come from the differences in the elongation and triangularities or other differences in the experimental equilibria. In order to isolate possible effects from these differences, an additional study for a set of analytical equilibria will be useful and is also considered. Such a scan is outside the scope of this research that has a focus on the experimental equilibria, and can be a subject of future research. However, even though there are possible effects of anomalous transport and plasma current, the coupled neoclassical-MHD stability simulations yield valuable insights regarding the effects of elongation and triangularity on the pedestal width of different plasma profiles. The results of the simulations carried out can provide additional leverage in controlling the pedestal buildup, the bootstrap current in the pedestal region, and the stability of the H-mode pedestal and are not obtained with either

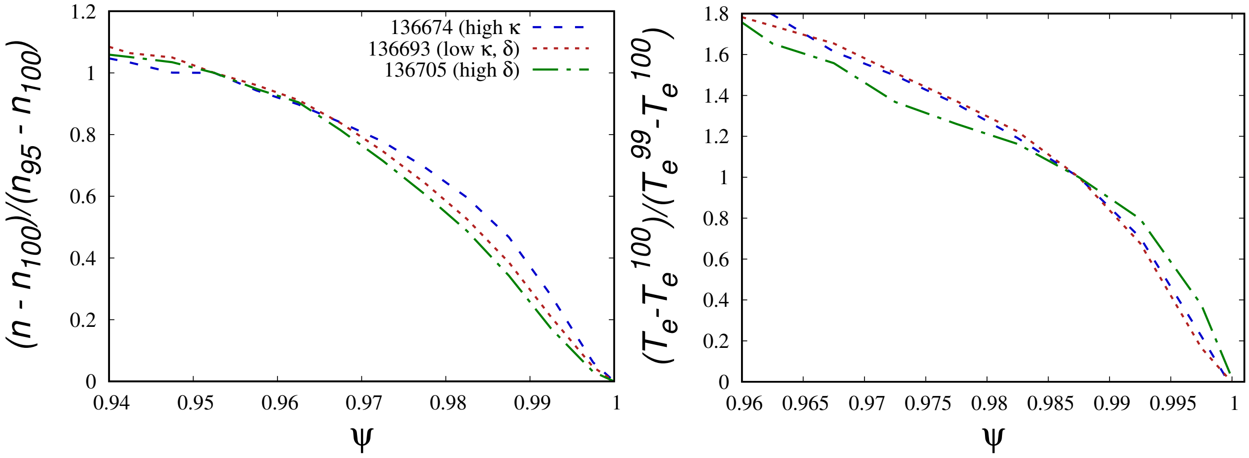

FIG. 9. (Color online) Normalized plasma density and normalized temperature profiles as functions of normalized poloidal flux (ψ) for DIII-D discharges with low and high elongations and with low and high triangularities. Here, n_{100}, T_{e}^{100}, n_{95} and T_{e}^{95} are the plasma densities and electron temperatures at the separatrix and at 95% of the normalized poloidal flux, respectively.

the XGC0 or ELITE codes when they used separately. The discovered dependence of the pedestal width confirms the importance of the coupled neoclassical/MHD stability dynamics in the description of the H-mode pedestal.

III. EXTENDING THE VALIDATION OF MULTI-MODE MODEL FOR ANOMALOUS TRANSPORT TO HIGH POLOIDAL BETA DIII-D DISCHARGES

In this research, the Multi-Mode Model (MMM7.1) for anomalous transport[40] is tested in predictive modeling of temperature profiles of high poloidal beta discharges in DIII-D. The importance of reliable predictions of plasma profiles is related to the development of new operational scenarios and to the prediction of plasma performance in future tokamaks such as ITER. A robust and reliable model for anomalous transport is also important for real-time control techniques and for understanding the role of various transport mechanisms in tomakak plasmas. Independent of the fidelity level, each model has its range of applicability. The analytical assumptions that are utilized in the model development provide some guidance for the ranges of model applicability. However, the ultimate test for model applicability ranges can provide only a careful validation of model results in different plasma parameter regimes. The Multi-Mode Model has been previously validated in the most conventional plasma regimes including the Ohmic, low- and high- confinement modes[23,54]. A new H-mode plasma regime with high poloidal betas and high plasma currents has been recently studied in the DIII-D tokamak[55,56]. This regime is characterized by a high bootstrap current fraction and steady-state operation without extensive external control. Typically, these discharges have internal transport barriers at large radius and large betas with $\beta_p > 4$ and $\beta_N \approx 4$. This discharge scenario is promising for achieving improved core confinement with reduced NBI torque. Previously, the MMM7.1 model has not been tested for the discharge scenarios of this type and this report describes first validation results of the MMM7.1 model for high beta poloidal DIII-D discharges.

The MMM7.1 consists of a combination of contributions from different transport theories.

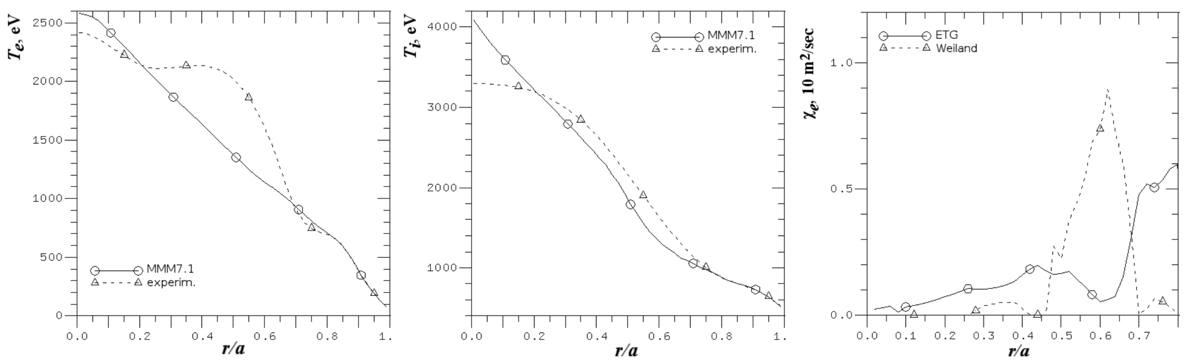

(a) (b) (c)

FIG. 10. Results of predictive modeling of high poloidal beta DIII-D discharge 154406 using the Weiland and ETG components of MMM7.1. The predicted electron (a) and ion (b) temperature profiles are compared with the experimental profiles. The effective electron thermal diffusivities from the Weiland (dashed curve) and ETG (solid curve) components of MMM7.1 are shown in panel (c).

It includes the Weiland module for ion temperature gradient modes, trapped electron modes and collision dominated MHD modes[57], the Rafiq module for drift-resistive-inertial ballooning modes (DRIBM)[37] and the Horton module with the Jenko threshold[58] for anomalous transport driven by Electron Temperature Gradient (ETG) modes. The MMM7.1 model is used in the computation of thermal, particle and toroidal angular momentum transport.

The role of different modes described by MMM7.1 is investigated in this research. In particular, the temperature profiles for a number of high-poloidal beta DIII-D discharges are predicted using the Weiland and ETG components of MMM7.1. The predicted temperature profiles are compared to the corresponding temperature profiles from interpretive TRANSP simulations. Fig. 10 shows the predicted electron and ion temperature profiles for the DIII-D discharge 154406. Reasonable agreement between predicted and experimental profiles is observed. However, the location of internal transport barrier can not be accurately reproduced in the predictive MMM7.1 simulations. The reason is a rather significant electron thermal transport from the Weiland and ETG components of MMM7.1 that destroys ITB from strong off-axis ECR heating (see Fig. 10c). The effect from the DRIBM model is also investigated. The DRIBM modes are expected to be stable in the plasma core region of H-mode discharges. However, PTRANSP analysis of the DIII-D discharge 154406 shows that there is significant transport predicted by DRIBM in the region from 0.3 to 0.7 of normalized minor radius (see Fig. 11a). The electron temperature in this PTRANSP simulation is found noticeably below the experimental values (see Fig. 11b). The DRIBM model includes contributions from other MHD modes in addition to the drift resistive ballooning modes that can be unstable in this region. This validation study suggests the DRIBM predicts a significantly larger level of electron transport than expected. In this research, possible effects that can contribute to stabilization of these modes, for example, effects associated with the large poloidal beta such as the Shafranov shift stabilization in the MMM7.1 model, are discussed.

The effect of Shafranov shift is investigated using a numerical scan in the MMM7.1 model. The Shafranov shift effect in MMM7.1 is included through a geometric factor modifying the ion magnetic drift frequency, which varies strongly around each magnetic surface:

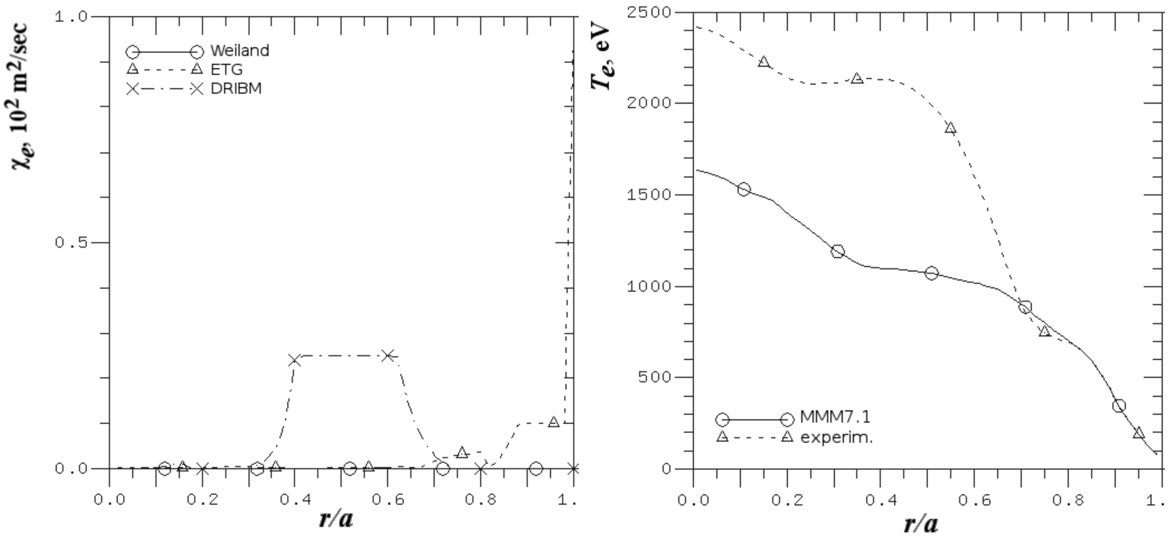

FIG. 11. Results of predictive modeling of high poloidal beta DIII-D discharge 154406 using the Weiland, ETG, and DRIBM components of MMM7.1. The effective electron thermal diffusivities from the Weiland, ETG, and DRIBM components of MMM7.1 are shown in panel (a). The predicted and experimental temperature profiles are compared in panel (b).

$$\omega_{Dj} = \frac{-2k_\theta T_j}{Z_j eBR}\left(\cos\theta + s\theta\sin\theta + \alpha_m \sin^2\theta\right),$$

where j is the ion specie index, Z is the ion charge, k_θ is the wave vector in the poloidal direction, s is the magnetic shear, and α_m is the alpha MHD which is defined as

$$\alpha_m = \frac{2\mu_0 R q^2}{B^2}\frac{dp}{dr}$$

.

The alpha MHD is proportional to the Shafranov shift and the effect of the Shafranov shift can be investigated by introducing a scaling factor for the last term in the first equation above:

$$\omega_{Dj} = \frac{-2k_\theta T_j}{Z_j eBR}\left(\cos\theta + s\theta\sin\theta + C^{(4)}_{\mathrm{MMM}}\alpha_m \sin^2\theta\right)$$

.

The coefficient $C^{(4)}_{\mathrm{MMM}}$ is added to the MMM7.1 module namelist. Five values of $latexC^{(4)}_{\mathrm{MMM}}$ are tested and are shown in Fig. 12:
$C^{(4)}_{\mathrm{MMM}} = 0.0$ - simulation 154406A51 (dashed curve with triangles)
$C^{(4)}_{\mathrm{MMM}} = 0.5$ - simulation 154406A52 (dash-dotted curve with crosses)
$C^{(4)}_{\mathrm{MMM}} = 1.0$ - simulation 154406A30 (solid curve with circles)
$C^{(4)}_{\mathrm{MMM}} = 2.0$ - simulation 154406A53 (dashed curve with squares)
$C^{(4)}_{\mathrm{MMM}} = 4.0$ - simulation 154406A54 (dashed curve with circles)

The Shafranov shift has stabilizing effect on electron and ion channels of transport. However, the effect on the electron channel is somewhat weaker. Also, the large spike in transport in the ITB region in the electron thermal diffusivities is found weakly affected by the Shafra-

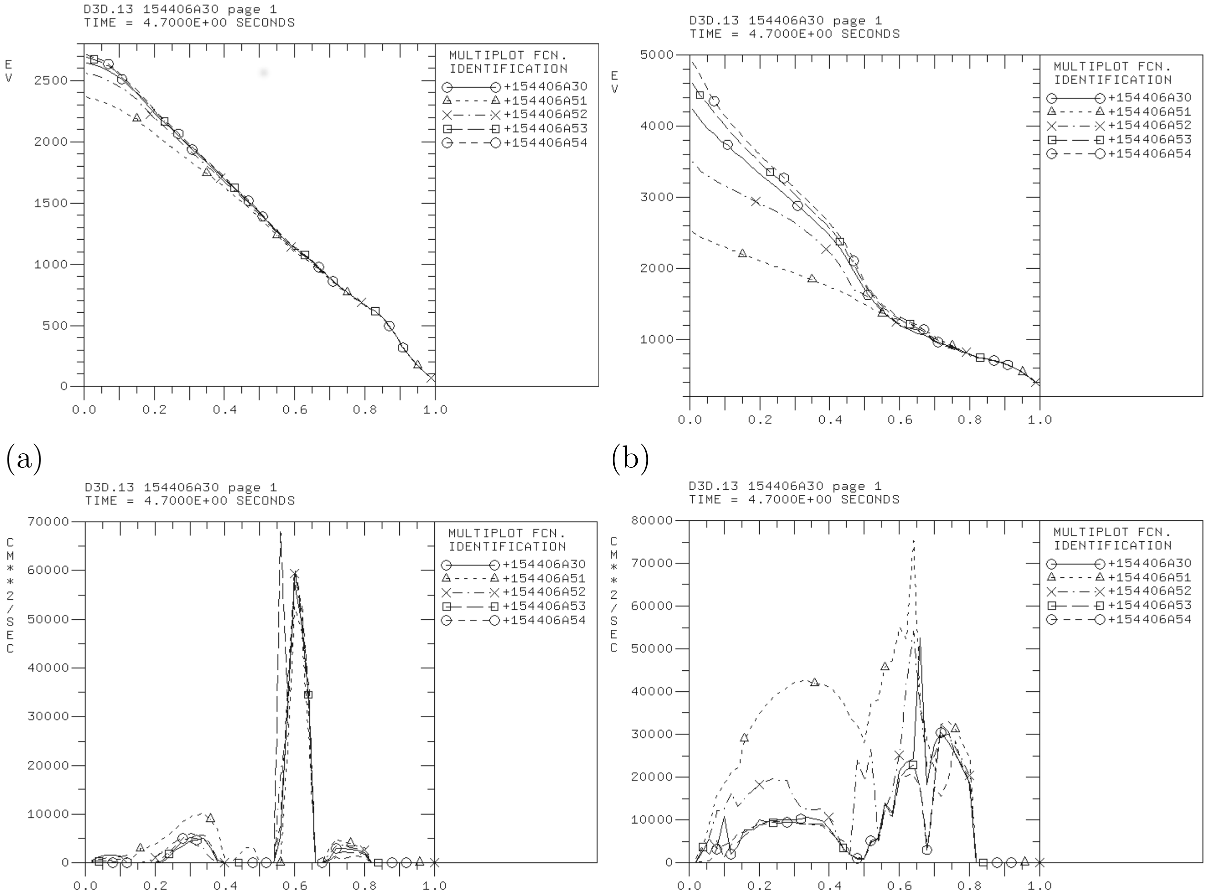

(a) (b)

(c) (d)

FIG. 12. Top panels: Electron and ion temperature profiles for different values of Shafranov shift scaling factor. Bottom panels: Electron and ion thermal diffusivities for different values of Shafranov shift scaling factor $C^{(4)}_{\rm MMM}$.

nov shift.

The results of this research have been presented at the IAEA FEC in Kyoto[6].

IV. VERIFICATION STUDIES OF ANOMALOUS TRANSPORT USING THE GYRO-KINETIC GTC CODE

During the last year of the project, the anomalous trasnport in high beta poloidal DIII-D discharges has been verified using the gyro-kinetic GTC code. In order to verify and better understand the nature of anomalous transport in high beta poloidal DIII-D discharges, a verification with higher fidelity anomalous transport codes can be beneficial. In this report, first results on the verification of MMM7.1 and GTC results are presented. The GTC[59] code is a gyro-kinetic code with the ions that are treated by integrating the gyrokinetic equation along gyrocenter trajectories and the electrons described by the fluid-kinetic hybrid model[60,61]. The fluid-kinetic hybrid model is based on the separation of the electron response into a dominant adiabatic part $\delta f_e^{(a)}$ and non-adiabatic correction δh_e:

$$\delta f_e \equiv \delta f_e^{(a)} + \delta h_e = \frac{e f_0}{T_e}\delta\phi_{\text{eff}} + \left.\frac{\partial f_0}{\partial\psi}\right|_{v_\perp}\delta\psi + \delta h_e, \tag{2}$$

where f_0 is the equilibrium local Maxwellian distribution, T_e is the equilibrium electron temperature, ψ and $\delta\psi$ is the equilibrium and perturbed poloidal magnetic flux, respectively. The effective potential $\delta\phi_{\text{eff}}$ determines the parallel electric field as $\delta E_\parallel = -\nabla_\parallel\delta\phi_{\text{eff}}$. In electrostatic simulations $\delta\phi_{\text{eff}}$ becomes the electrostatic potential $\delta\phi$ obtained by solving the gyrokinetic Poisson's equation, while $\delta\psi$ vanishes. The non-adiabatic (kinetic) correction δh_e is obtained by integrating the electron drift-kinetic equation subtracted by the adiabatic free streaming terms. The fluid-kinetic hybrid electron model provides an excellent numerical efficiency while preserving the essential kinetic effects.

GTC employs magnetic Boozer coordinates for particle dynamics, and unstructured field-aligned mesh for the field solvers. Realistic magnetic equilibrium provided by the EFIT code and experimental plasma profiles are used.

In all GTC simulations the convergence in time/space resolution and number of particles is achieved. In this work a typical number of macro-particles per cell for both electron and ion species is 40, the time step is $\Delta t\Omega_{ci} \approx 5$. The spatial resolution is $\Delta r/\rho_i \approx r\Delta\theta/\rho_i \approx 0.5$, and 32 grid points in the toroidal directions are required to resolve the parallel field variations. The perturbed potentials are calculated assuming homogeneous Dirichlet radial boundary conditions.

The objective of this first verification test is to understand the modes that drive the transport in the region of internal transport barrier. The flux averaged effective diffusivities computed using the GTC code for the plasma profiles at 5.1 sec are shown in Fig. 13. The diffusivities are increased towards the ITB region of the discharge. There is no anomalous transport predicted with GTC inside $\rho = 0.5$. Comparing the electron thermal diffusivities computed with the MMM7.1 with the electron thermal diffusivity computed with the GTC code (Fig. 13), one can notice that the transport computed with both models has a qualitatively similar behavior. The electron thermal diffusivities spike inside ITB to approximately 0.7-0.9 m^2/s and the ion thermal diffusivity is found to reach 1.4 m^2. Both the electron and ion thermal transport are found to be driven by the ITG modes. The GTC code produces significantly lower levels of transport comparing to the transport computed with the MMM7.1 model, which might be an indication of differences in the model stiffness. The MMM7.1 also computes some other MHD modes that are not considered in this first validation excersize. This can explain the difference in the ion thermal transport in the core region with $r/a<0.55$. The simulation of ETG turbulence is much more expensive and it was not included in this first verification comparison study. The comparison of the ETG driven transport will be considered in future work. Possible role of kinetic ballooning modes has be tested with the GTC code. There is no significant level of kinetic ballooning modes inside ITB acording to GTC.

It should be noted that despite the differences in the effective diffusivities predicted with MMM7.1 and GTC, this first validation studies between these two codes can be considered as encouraging. The differences can be partially attributed to the differences in the simulations. The GTC simulations are performed in an interpretive way with the plasma profiles fixed in time, while the MMM7.1 simulations are predictive simulations that allow the plasma profiles to evolve. In spite these differences, both codes predicted comparable diffusivity trends.

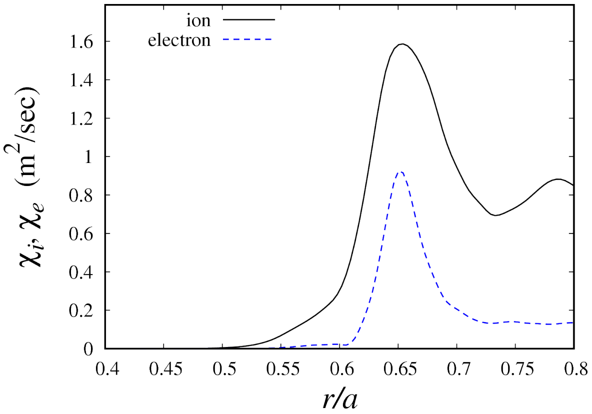

FIG. 13. The electron and ion effective diffusivities computed with GTC code for the DIII-D discharge 154406 at t=5.1 sec.

The ITG driven transport becomes unstable at r/a=0.5 in both codes, which might be an indication that both codes predict similar instability threshold. More detailed comparison of the two codes will include a comparison of stiffness of ITG and ETG driven transport in MMM7.1 and GTC.

V. MODELING OF POLOIDAL ROTATION PROFILES IN THE PLASMA CORE OF THE DIII-D TOKAMAK

Our previous studies of poloidal rotation profiles in tokamaks were extended to the modeling of the rotation profiles in the region of internal transport barriers (ITBs). In a number of experiments, significant deviations from the neoclassical poloidal velocity predictions are found [1-4]. We believe that these deviations can be partially explained by the neoclassical effects. In order to study the anomalous effects on the poloidal rotation profiles, the following simplified equation for the poloidal rotation is used in the integrated modeling ASTRA code:

$$\frac{\partial \langle v_\theta \rangle}{\partial t} = \nu_{\rm NC} \left(\langle v_\theta - v_\theta^{\rm NC} \rangle \right) - \frac{1}{m_i n_i V'} \frac{\partial}{\partial \rho} \left(V' P_\theta \right) + \frac{S_\theta^{\rm NBI}}{m_i n_i}, \tag{3}$$

where $\nu_{\rm NC}$ is the neoclassical damping coefficient, V is the plasma volume, $v_\theta^{\rm NC}$ is the poloidal velocity computed from the neoclassical theory, $S_\theta^{\rm NBI}$ is the poloidal torque associated with NBI, P_θ is defined as $P_\theta = -\langle \nabla \rho^2 \rangle \chi_\theta^{\rm eff} \partial v_\theta / \partial \rho$ using the effective poloidal momentum diffusivity $\chi_\theta^{\rm eff}$ computed in the MMM7.1 model. The contribution from NBI poloidal torque has been neglected in this study. The second term in the equation above represents the Reynolds stress related to the anomalous effects. In MMM7.1, the poloidal momentum transport is driven by the drift wave modes such as ITG and TEM modes. The Reynolds stress related effects are usually small and the first term in Eq. 3 dominates other terms. However, the contribution from the second term might become important in the regions of large plasma gradients. Depending on the ratio of the first two terms and the relative signs of $v_\theta^{\rm NC}$ and $\chi_\theta^{\rm NC}$, the anomalous effects can either increase or decrease the neoclassical poloidal rotation. The effect is particularly strong in the regions of large plasma gradients such inside of ITBs. The poloidal rotation profiles that were found using the neoclassical NCLASS code and using Eq. 3 are compared to experimental profiles for several DIII-D discharges. It is found that the anomalous rotation reduces significantly the neoclassical poloidal rotation velocity in the ITB region of the DIII-D discharge 154485 as shown in Fig. 14.

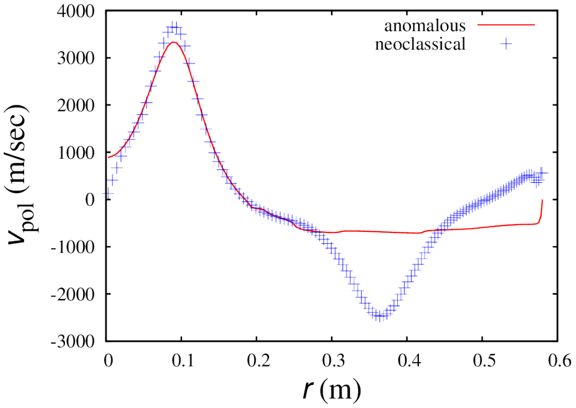

FIG. 14. Comparison of neoclassical poloidal rotation profile computed using the NCLASS module (crossed blue curve) and poloidal rotation profiles computed with anomalous effects included (solid red curve) for the DIII-D discharge 154485. The ITB pedestal region extends approximately from r=0.29 m to r=0.42 m. The anomalous effects contribute little to the poloidal rotation outside of the ITB region. These effects significantly reduce the poloidal rotation inside of ITB for this discharge.

We are currently formulating an improved equation for the poloidal momentum transport that can be implemented in the FACETS code.

VI. DEVELOPMENT AND IMPLEMENTATION OF UNCERTAINTY QUANTIFICATION METHODS FOR THE INTEGRATED MODELING CODES

The objective of this task is to develop methods that can be used for routine analysis of experimental data in interpretive modeling codes and for validation of transport models in the predictive transport modeling codes. As a testbed for this task the TASK3D-a1 code has been used. This work is primarily performed during the PI visit to the National Institute for Fusion Studies in Toki, Japan in collaboration with Drs. M. Yokoyama, R. Seki, and C. Suzuki. The PI implemented the DAKOTA toolkit[62] in the TASK3D-a1 code. The DAKOTA toolkit is being developed at the Sandia National Laboratory, and it can be used for uncertainty quantification, sensitivity analysis, optimization, and calibration studies. The DAKOTA toolkit is currently being implemented in a number of integrated modeling and plasma simulation codes including the interpretive and predictive integrated modeling TRANSP code, predictive modeling FACETS code, and the suite of gyro-kinetic XGC codes. The implementation of the DAKOTA package in TASK3D-a1 can be used for (1) the computation of error bars for all quantities derived in the interpretive analysis; (2) separation of errors that are associated with raw experimental errors and errors related to numerical analysis of experimental data such as numerical fitting, interpolation, and smoothing; (3) validation of theory-based models; (4) sensitivity analysis of theory-based models; and (5) development of empirical scaling laws from interpretive experimental data. These applications are closely related to the main objective of any interpretive modeling code, which is the development of an improved understanding of physics processes in burning plasma. Such

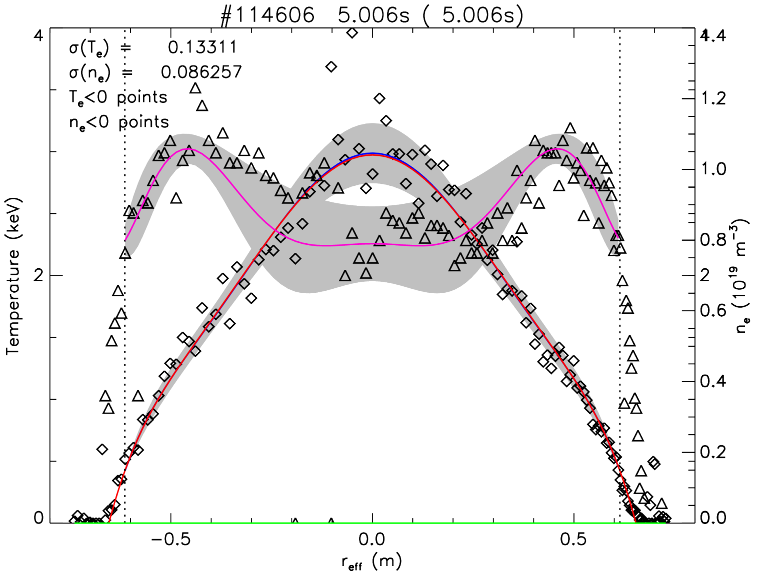

FIG. 15. The red solid curve shows the fitted electron temperature profile and the purple solid curve shows the fitted electron density profiles. The raw experimental data are shown as triangles from the electron density profile and as diamonds for the electron density profile. The uncertainty ranges in the fitting of experimental data associated with the experimental error bars is shown as gray regions.

understanding can be achieved through the analysis of scaling laws found in experimental data, and the development and testing of analytical models. The model validation process that computes the validation metric is a key aspect in the testing of new analytical models. Integrated modeling codes with predictive capabilities can also be used for the validation of theory-based models. When the analytical models are validated, they can be used for predictive analysis of future discharges. After the predictive capabilities in the TASK3D-a1 code will be developed, the new DAKOTA/TASK3D-a1 coupling capabilities can be used for the validation of theory-based models in predictive simulations, the optimization of the existing discharge scenarios, and for the development of new discharge scenarios.

Most experimental data in the TASK3D-a code is being fitted using three and four order polynomials. The fitting coefficients are being shared between different modules of TASK3D-a using external files and common blocks. The fitting algorithms in TASK3D-a1 have been updated by weighted fittings with the weights that are inversely proportional to the experimental error bars. In these fittings, the experimental data that have larger error bars will have smaller contributions to the polynomial fitting. This definitions of the experimental data fitting weights exclude the experimental temperature data points with the experimental errors that exceed 500 eV and the electron density experimental data points with errors that exceed $2.0 \times 10^{20}/m^3$. The data points with large errors also have significantly reduced weights.

The fitted experimental profiles for the electron temperature and density are compared with the raw experimental data in Fig. 15. We have found that the use of weighted fitting with the weights that depend on the experimental error bars changes the fitting originally implemented in TASK3D-a1. In particular, the change is noticeable for the electron density profiles in the plasma core region.

An option to control the fitting profiles within the experimental uncertainty region is

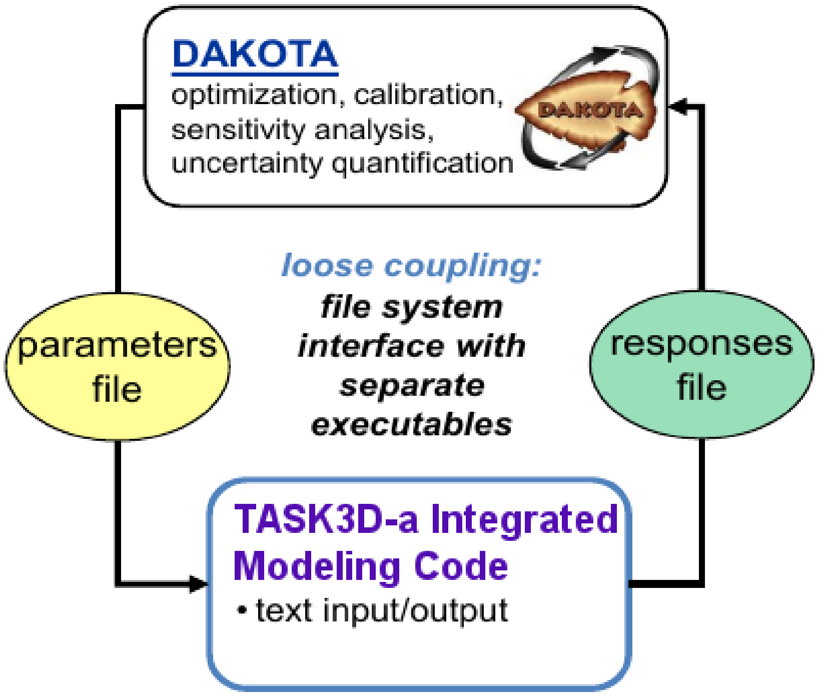

FIG. 16. The TASK3D/DAKOTA computation loop. The DAKOTA toolkit generates the input files to TASK3D-a1 and process the output from TASK3D-a1.

implemented in TASK3D-a1 through a set of fitting coefficients that are controlled by DAKOTA as described below. The DAKOTA toolkit and TASK3D-a1 code are coupled so that DAKOTA can control the TASK3D-a1 input and process the TASK3D-a1 output as shown in Fig. 16.

The effect of the experimental data uncertainty on the effective electron and ion thermal diffusivity is shown in Fig. VI. The gray areas show the uncertainty ranges in the computation of the effective thermal diffusivities, and the solid curves show the effective diffusivities computed with the DAKOTA fitting parameters set to zero. These results are generated using a simplified DAKOTA input file. This is why the solid curve is found outside of gray regions for some $r_{\rm eff}$.

The computation of ranges in the effective diffusivities, fluxes and other output profiles and plasma parameters can be important for:

- Analysis of experimental data where the error bars are being propagated to all derived quantities;
- Comparison of interpretive analysis runs of various discharges;
- Investigation of the uncertainties that originate from experimental errors of different physics quantities;
- Comparison of numerical errors such as those that originate from fitting errors and errors that originate from experimental errors of measured quantities;
- Verification and validation of physics models using the interpretive integrated modeling code.

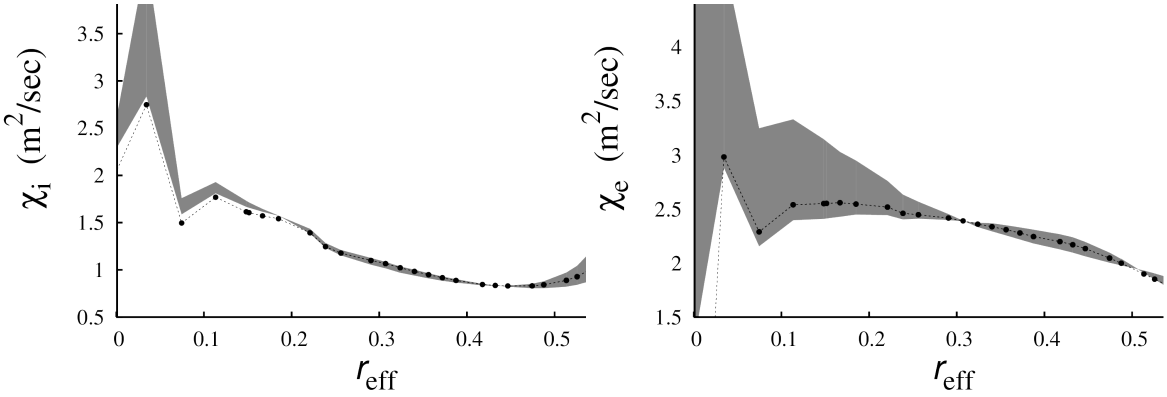

FIG. 17. The left panel shows the ion thermal diffusivity profile as a function of r_{eff} for the LHD discharge 114606. The right panel shows the corresponding electron thermal diffusivity profile. The gray areas show the uncertainty ranges in the computation of effective diffusivities that correspond to the uncertainties in the experimental data. The solid curves show the effective diffusivities computed with the DAKOTA fitting parameters set to zero.

These tasks are the sample tasks that can be done with the existing DAKOTA/TASK3D-a1 coupling. The coupling of DAKOTA and TASK3D-a1 codes can be used for the extended verification and validation of physics models, for the optimization of existing discharge scenarios, and for the development of new discharge scenarios. However, these tasks require some additional developments on the TASK3D-a1 side.

VII. INVESTIGATING THE EFFECTS OF THE PEDESTAL HEIGHT AND WIDTH ON THE PLASMA CONFINEMENT IN ITER

The PI has contributed to the collaborative research that is being performed by the members of ITPA-IOS group. The objective of this research project is to access the operational space for long pulse scenarios ($\Delta t_{\text{burn}} \sim 1000\ s$, $Q \geq 5$) of ITER. In this project, a selection of 1.5D core transport models are used. The PI has provided results obtained using the MMM95, MMM7.1 and Weiland models. These simulations use improved boundary conditions that were obtained from a parametric scan from the EPED1 and SOLPS codes. For this scan, the EPED1 code was modified to take into account boundary conditions predicted by SOLPS for ITER. In contrast to the standard EPED1 assumptions, EPED1 with the SOLPS boundary conditions predicts no degradation of the pedestal pressure as density is reduced. Lowering the plasma density to $n_e \sim 5 - 6 \times 10^{19}\ m^{-3}$ leads to an increased plasma temperature, which reduces the loop voltage and increases the duration of the burn phase to $\Delta t_{\text{burn}} \sim 1000\ s$ with $Q \geq 5$ for $I_p \geq 13\ MA$ at moderate normalized pressure. The predictions for fusion gain are compared in Fig. 18. It is demonstrated that fusion gain $Q \geq 5$ with burn lengths of $\Delta t_{\text{burn}} \geq 800\ s$ can be achieved with the usual H-mode energy confinement enhancement HH98(y,2)∼1 for all models even for a plasma current as high as $Ip = 15\ MA$. These ITER plasmas require the same level of additional heating power as the reference $Q = 10$ inductive scenario at 15 MA (33 MW NBI and 17-20 MW EC heating and current drive power). However, unlike the “hybrid” scenarios considered previously, these H-mode plasmas neither require specially shaped q-profiles

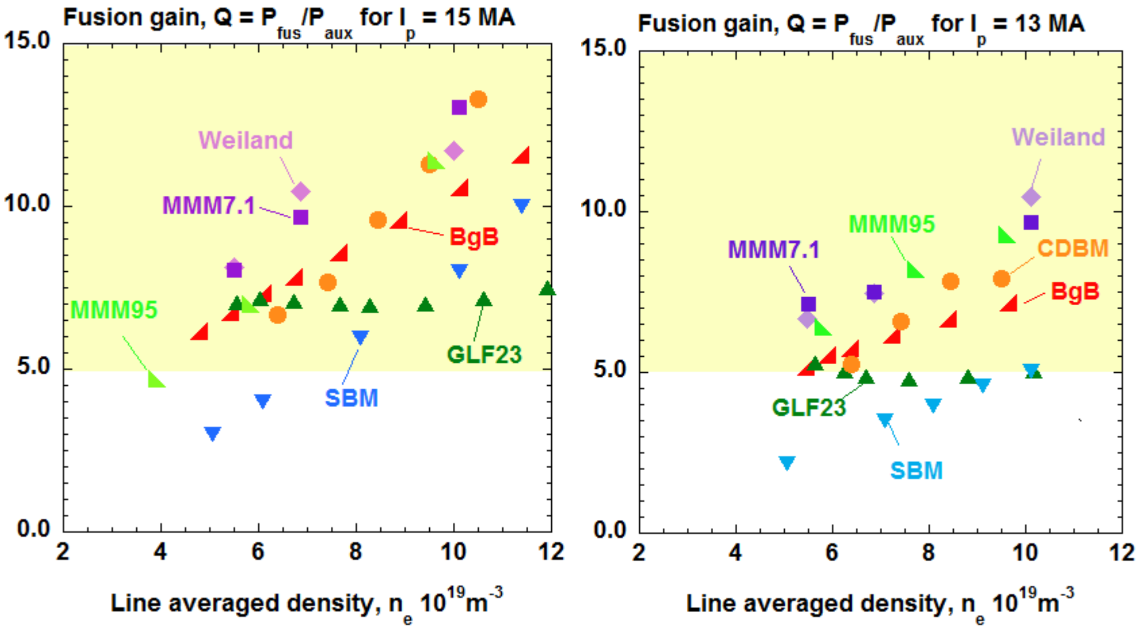

FIG. 18. Comparison of the predicted fusion Q for ITER plasmas with $I_p = 15\ MA$ (left panel) and $I_p = 13\ MA$ (right panel). The results from MMM95, MMM7.1 and Weiland models are compared with the results from the CDBM, GLF23, Bohm/GyroBohm (BgB), and Scaling-Based models.

nor improved confinement in the core for the transport models considered in this study. These medium density H-mode plasma scenarios with $I_p \geq 13\ MA$ present an attractive alternative to hybrid scenarios to achieve ITER long pulse $Q \geq 5$ scenario and deserve further analysis and experimental demonstration in present tokamaks.

[1] A. Pankin, J. Hughes, M. Greenwald, A. Kritz, T. Rafiq, and the EPSI Team. Interpretive analysis of residual anomalous transport in the H-mode pedestal region of Alcator C-Mod tokamak. In Proc. of Transport Task Force Meeting (April 28-May 1, 2015; Salem, MA), 2015.

[2] A. Pankin, J. Hughes, M. Greenwald, A. Kritz, T. Rafiq, and the EPSI Team. Anomalous transport in the Alcator C-Mod H-mode pedestal. In Proc. of H-mode workshop (October 19-21, 2015, Garching, Germany), 2015.

[3] A.H. Kritz, T. Rafiq, A.Y. Pankin, J. Hughes, and M. Greenwald. Validation of MMM7.1 and TGLF anomalous transport models for predicting the evolution of Alcator C-Mod temperature profiles. In Proc. of 57th APS DPP Annual meeting (November 16-50, 2015, Savannah, GA), page CP12.00006, 2015.

[4] A. Pankin, J. Hughes, M. Greenwald, A. Kritz, and T. Rafiq. Anomalous transport in the H-mode pedestal of Alcator C-Mod discharges. Nuclear Fusion, 57:022012, 2017.

[5] A. Pankin, A. Garofalo, B. Grierson, A. Kritz, and T. Rafiq. Computational study of anomalous transport in high beta DIII-D discharges with ITBs. In Proc. of 57th APS DPP Annual meeting (November 16-50, 2015, Savannah, GA), page JP12.00084, 2015.

[6] A.Y. Pankin, A.M. Garofalo, B.A. Grierson, A.H. Kritz, and T. Rafiq. Extending the validation of Multi-Mode Model for anomalous transport to high poloidal beta DIII-D discharges. Proc. of the 26th IAEA Fusion Energy Conference (Kyoto, Japan), 2016.

[7] A.Y. Pankin, I. Holod, A. Garofalo, and J. Weiland. Understanding and prediction of internal transport barriers in tokamaks using inte-

grated modeling. In Proc. of 44th International Conference on Plasma Science (May 21-25, Atlantic City, NJ), pages WE–2.2–2, 2017.

[8] A.Y. Pankin, A.M. Garofalo, A.H. Kritz, T. Rafiq, and J. Weiland. Anomalous transport in high beta poloidal DIII-D discharges. In Proc. of 21st Joint EU-US Transport Task Force Meeting (Leysin, Switzerland; 5-8 September), 2016.

[9] A.Y. Pankin, I. Holod, A. Garofalo, and J. Weiland. Understanding and prediction of internal transport barriers in tokamaks using integrated modeling. In Proc. of 2017 US-EU Transport Task Force Meeting (April 25-28; Williamsburg, VA), 2017.

[10] A.M. Garofalo, X. Gong, S. Ding, J. Huang, J. McClenaghan, C. Pan, J. Qian, Q. Ren, G.M. Staebler, J. Chen, L. Cui, B.A. Grierson, J.M. Hanson, C.T. Holcomb, X. Jian, G. Li, M. Li, A.Y Pankin, Y. Peysson, X. Zhai, P.T. Bonoli, D.L. Brower, W. Ding, J.R. Ferron, W. Guo, L.L. Lao, K. Li, H. Liu, B. Lyu, G. Xu, and Q. Zang. Joint DIII-D/EAST research on the development of a high poloidal beta scenario for the steady state missions of ITER and CFETR. Accepted for publication in Plasma Phys. Controlled Fusion, 2017.

[11] A.Y. Pankin, I. Holod, A. Garofalo, and J. Weiland. Extending the validation of Multi-Mode model for anomalous transport to high beta poloidal tokamak scenario in DIII-D. Submitted for publication in Physics of Plasmas, 2017.

[12] A.Y. Pankin, T. Rafiq, A.H. Kritz, G.Y. Park, P.B. Snyder, and C.S. Chang. Investigation of the plasma shaping effects on the H-mode pedestal structure using coupled kinetic neoclassical/MHD stability simulations. Physics of Plasmas, 24:062502, 2017.

[13] A.Y. Pankin, T. Rafiq, A.H. Kritz, G.Y. Park, C.S. Chang, D. Brunner, R.J. Groebner, J.W. Hughes, B. LaBombard, J.L. Terry, and S. Ku. Kinetic modeling of divertor heat load fluxes in the Alcator C-Mod and DIII-D tokamaks. Phys. Plasmas, 22:092511, 2015.

[14] A.H. Kritz, J. Ma, G. Wang, J. Weiland, T. Rafiq, and A.Y. Pankin. Modeling of particle flux reversal in Tore Supra and EAST tokamaks. In Proc. of Int. Conference of Numerical Simulations in Plasmas (ICNSP, August 12-14, 2015, Golden, CO), 2015.

[15] Yong-Su Na, C.E. Kessel, D.H. Na, A. Fukuyama, J. Garcia, N. Hayashi, K. Kim, F. Koechl, T. Luce, A. Pankin, J.M. Park, A.R. Polevoi, F. Poli, A.C.C. Sips, I. Voitsekhovitch, A. Wisitsorasak, and X. Yuan. On benchmarking of particle transport simulations in ITER. Proc. of the 26th IAEA Fusion Energy Conference (Kyoto, Japan), 2016.

[16] A.Y. Pankin, M. Yokoyama, R. Seki, C. Suzuki, S.E. Kruger, A. Hakim, A.H. Kritz, T. Rafiq, CPES (EPSI), FACETS, and CSWIM teams. Advanced techniques in interpretive andpredictive transport analysis of burning plasmas: Progress towards the implementation of uncertainty quantification and sensitivity analysis tools in the TASK3D code. In Proc. of NIFS Simulation Symposium (September 10-11, Toki, Japan), 2014.

[17] A.Y. Pankin, A.H. Kritz, S.E. Kruger, and T. Rafiq. Advances in whole-device integrated modeling of tokamak plasmas. In Proc. of International Conference on Plasma Science and Applications (September 22-24, Kathmandu), 2014.

[18] A. Pankin, M. Yokoyama, R. Seki, C. Suzuki, A. Kritz, and T. Rafiq. Use of uncertainty quantification techniques for interpretive and predictive transport analysis of burning plasmas. In Proc. of APS DPP Meeting (October 27-31, New Orleans, LA), page JO3.00009, 2014.

[19] M. Yokoyama, R. Seki, C. Suzuki, M. Sato, A. Shimizu, M. Emoto, S. Murakami, M. Osakabe, T.Ii. Tsujimura, Y. Yoshimura, K. Ogawa, S. Satake, Y. Suzuki, T. Goto, K. Ida, N. Pablant, D. Gates, A.Y. Pankin, F. Warmer, P. Vincenzi, Numerical Simulation Reactor Research Project, and LHD Experiment Group. Extended capability of the integrated transport analysis suite, task3d-a, for lhd experiment, and its impacts on facilitating stellarator-heliotron research. Proc. of the 26th IAEA Fusion Energy Conference (Kyoto, Japan), 2016.

[20] A.H. Kritz, V. Tangri, T. Rafiq, and A.Y. Pankin. Numerical analysis of drift resistive inertial ballooning modes. In Proc. of APS DPP Meeting (October 27-31, New Orleans, LA), page BP8.00054, 2014.

[21] T. Rafiq, A.H. Kritz, A.Y. Pankin, and X. Yuan. Predictive modeling of tokamak density, temperature and toroidal rotation profiles. In Proc. of APS DPP Meeting (October 27-31, New Orleans, LA), page BP8.00060, 2014.

[22] V. Tangri, T. Rafiq, A.H. Kritz, and A.Y. Pankin. Numerical analysis of drift resistive inertial ballooning modes. Phys. Plasmas, 21:092512, 2014.

[23] T. Rafiq, A.H. Kritz, V. Tangri, A.Y. Pankin, I. Voitsekhovitch, R.V. Budny, and JET EFDA Contributors. Integrated modeling of temperature profiles in L-mode tokamak discharges. Phys. Plasmas, 21:122505, 2014.

[24] T. Rafiq, J. Weiland, A.H. Kritz, L. Luo, and A.Y. Pankin. Microtearing modes in tokamak discharges. Phys. Plasmas, page 062507, 2016.

[25] A.R. Polevoi, A. Loarte, N. Hayashi, H.S. Kim, S.H. Kim, F. Koechl, A.S. Kukushkin, V.M. Leonov, S.Yu. Medvedev, M. Murakami, Y.S. Na, A.Y. Pankin, J. M. Park, P.B. Snyder, J.A. Snipes, V.E. Zhogolev, and the IOS ITPA TG. Assessment of operational space for long-pulse scenarios in ITER. Nucl. Fusion, 55:063019, 2015.

[26] T. Rafiq, A.H. Kritz, C.E. Kessel, and A.Y. Pankin. Fusion power production in International Thermonuclear Experimental Reactor baseline H-mode scenarios. Phys. Plasmas, 22:042511, 2015.

[27] A.H. Kritz, T. Rafiq, C.E. Kessel, and A.Y. Pankin. Fusion power production in ITER baseline H-mode scenarios. In Proc. of Transport Task Force Meeting (April 28-May 1, 2015; Salem, MA), 2015.

[28] M.V. Umansky, A.Y. Pankin, T.D. Rognlien, A.M. Dimits, A. Friedman, and I. Joseph. Status of parallel python-based implementation of UEDGE. In Proc. of 59th Annual Meeting of the APS Division of Plasma Physics (October 23-27; Milwaukee, WI), page YP11.00022, 2017.

[29] M. Sugihara, Yu. Igitkhanov, G. Janeschitz, A. E. Hubbard, Y. Kamada, J. Lingertat, T. H. Osborne, and W. Suttrop. A model for H mode pedestal width scaling using the International Pedestal Database. Nucl. Fusion, 40:1743–1755, 2000.

[30] B.N. Rogers and J. F. Drake. Diamagnetic stabilization of ideal ballooning modes in the edge pedestal. Phys. Plasmas, 6:2797, 1999.

[31] J.D. Callen. Paleoclassical transport in low-collisionality toroidal plasmas. Phys. Plasmas, 12:092512, 2005.

[32] J.D. Callen, R.J. Groebner, T.H. Osborne, J.M. Canik, L.W. Owen, A.Y. Pankin, T. Rafiq, T.D. Rognlien, and W.M. Stacey. Analysis of pedestal plasma transport. Nucl. Fusion, 50:064004, 2010.

[33] A.Y. Pankin, S. Kruger, R.J. Groebner, A. Hakim, A.H. Kritz, and T. Rafiq. Validation of anomalous transport models using additive flux minimization technique. Phys. Plasmas, 20:102501, 2013.

[34] T. Onjun, G. Bateman, A.H. Kritz, and G. Hammett. Models for the pedestal temperature at the edge of H-mode tokamak plasmas. Phys. Plasmas, 9:5018, 2002.

[35] P.B. Snyder, R.J. Groebner, J.W. Hughes, T.H. Osborne, M. Beurskens, A.W. Leonard, H.R. Wilson, and X.Q. Xu. A first-principles predictive model of the pedestal height and width: development, testing and ITER optimization with the EPED model. Nucl. Fusion, 51:103016, 2011.

[36] R.J. Groebner, C.S. Chang, J.W. Hughes, R. Maingi, P.B. Snyder, X.Q. Xu, J.A. Boedo, D.P. Boyle, J.D. Callen, J.M. Canik, I. Cziegler, E.M. Davis, A. Diallo, P.H. Diamond, J.D. Elder, D.P. Eldon, D.R. Ernst, D.P. Fulton, M. Landreman, A.W. Leonard, J.D. Lore, T.H. Osborne, A.Y. Pankin, S.E. Parker, T.L. Rhodes, S.P. Smith, A.C. Sontag, W.M. Stacey, J. Walk, W. Wan, E.H.-J. Wang, J.G. Watkins, A.E. White, D.G. Whyte, Z. Yan, E.A. Belli, B.D. Bray, J. Candy, R.M. Churchill, T.M. Deterly, E.J. Doyle, M.E. Fenstermacher, N.M. Ferraro, A.E. Hubbard, I. Joseph, J.E. Kinsey, B. LaBombard, C.J. Lasnier, Z. Lin, B.L. Lipschultz, C. Liu, Y. Ma, G.R. McKee, D.M. Ponce, J.C. Rost, L. Schmitz, G.M. Staebler, L.E. Sugiyama, J.L. Terry, M.V. Umansky, R.E. Waltz, S.M. Wolfe, L. Zeng, and S.J. Zweben. Improved understanding of physics processes in pedestal structure, leading to improved predictive capability for ITER. Nuclear Fusion, 53(9):093024, 2013.

[37] T. Rafiq, G. Bateman, A.H. Kritz, and A.Y. Pankin. Development of drift-resistive-inertial ballooning transport model for tokamak edge plasmas. Phys. Plasmas, 17:082511, 2010.

[38] A. Mosetto, F.D. Halpern, S. Jolliet, J. Loizu, and Paolo Ricci. Turbulent regimes in the tokamak scrape-off layer. Phys. Plasmas, 20:092308, 2013.

[39] B. LaBombard, J.E. Rice, A.E. Hubbard, J.W. Hughes, M. Greenwald, J. Irby, Y. Lin, B. Lipschultz, E.S. Marmar, C.S. Pitcher, N. Smick, S.M. Wolfe, S.J. Wukitch, and the Alcator Group. Transport-driven Scrape-Off-Layer flows and the boundary conditions imposed at the magnetic separatrix in a tokamak plasma. Nucl. Fusion, 44:1047, 2004.

[40] T. Rafiq, A.H. Kritz, J. Weiland, A.Y. Pankin, and L. Luo. Physics basis of Multi-Mode anomalous transport module. Phys. Plasmas, 20:032506, 2013.

[41] C.S. Chang, Seunghoe Ku, and H. Weitzner. Numerical study of neoclassical plasma pedestal in a tokamak geometry. Phys. Plasmas, 11:2649–2667, 2004.

[42] M. Greenwald. Verification and validation for magnetic fusion. Phys. Plasmas, 17:058101, 2010.

[43] B.M. Adams, W.J. Bohnhoff, K.R. Dalbey, J.P. Eddy, M.S. Eldred, D.M. Gay, K. Haskell, P.D. Hough, and L.P. Swiler. Dakota, a multilevel parallel object-oriented framework for design optimization, parameter estimation, uncertainty quantification, and sensitivity analysis: Version 5.0 user's manual. Technical Report SAND2010-2183, Sandia National Laboratory, 2010.

[44] B. LaBombard, M.V. Umansky, R.L. Boivin, J.A. Goetz, J. Hughes, B. Lipschultz, D. Mossessian, C. S. Pitcher, and J. L. Terry. Cross-field plasma transport and main-chamber recycling in diverted plasmas on Alcator C-Mod. Nucl. Fusion, 40:2041–2060, 2000.

[45] B. LaBombard, R.L. Boivin, M. Greenwald, J. Hughes, B. Lipschultz, D. Mossessian, C.S. Pitcher, J.L. Terry, S.J. Zweben, and Alcator Group. Particle transport in the scrape-off layer and its relationship to discharge density limit in Alcator C-Mod. Phys. Plasmas, 8:2107, 2001.

[46] J. Cummings, A. Pankin, N. Podhorszki G. Park, S. Ku, R. Barreto, S. Klasky, C.S. Chang, H. Strauss, L. Sugiyama, P. Snyder, D. Pearlstein, B. Ludäscher, G. Bateman, A. Kritz, and the CPES Team. Plasma edge kinetic-MHD modeling in tokamaks using Kepler workflow for code coupling, data management and visualization. Communications in Computational Physics, 4:675–702, 2008.

[47] P.A. Schneider, E. Wolfrum, R.J. Groebner, T.H. Osborne, M.N.A. Beurskens, M.G. Dunne, B. Kurzan, T. Pütterich, E. Viezzer, the ASDEX Upgrade Team, the DIII-D Team, and JET EFDA Contributors. Analysis of temperature and density pedestal gradients in AUG, DIII-D and JET. Nuclear Fusion, 53(7):073039, 2013.

[48] P. B. Snyder, H. R. Wilson, J. R. Ferron, L. L. Lao, A. W. Leonard, T. H. Osborne, A. D. Turnbull, D. Mossessian, M. Murakami, and X. Q. Xu. Edge localized modes and the pedestal: A model based on coupled peeling-ballooning modes. Physics of Plasmas, 9(5):2037–2043, 2002.

[49] C. Holland, L. Schmitz, T. L. Rhodes, W. A. Peebles, J. C. Hillesheim, G. Wang, L. Zeng, E. J. Doyle, S. P. Smith, R. Prater, K. H. Burrell, J. Candy, R. E. Waltz, J. E. Kinsey, G. M. Staebler, J. C. DeBoo, C. C. Petty, G. R. McKee, Z. Yan, and A. E. White. Advances in validating gyrokinetic turbulence models against l- and h-mode plasmas a). Physics of Plasmas, 18(5), 2011.

[50] C.M. Greenfield, J.C. DeBoo, T.H. Osborne, F.W. Perkins, M.N. Rosenbluth, and D. Boucher. Enhanced fusion performance due to plasma shape modification of simulated ITER discharges in DIII-D. Nuclear Fusion, 37:1215, 1997.

[51] H Urano, Y Kamada, H Shirai, T Takizuka, H Kubo, T Hatae, and T Fukuda. Thermal energy confinement of high-triangularity elmy h-mode plasmas in jt-60u. Plasma Physics and Controlled Fusion, 44(1):11, 2002.

[52] P.B. Snyder, H.R. Wilson, J.R. Ferron, L.L. Lao, A.W. Leonard, D. Mossessian, M. Murakami, T.H. Osborne, A.D. Turnbull, and X.Q. Xu. Elms and constraints on the h-mode pedestal: peeling-ballooning stability calculation and comparison with experiment. Nuclear Fusion, 44(2):320, 2004.

[53] R.J. Groebner, A.W. Leonard, P.B. Snyder, T.H. Osborne, C.F. Maggi, M.E. Fenstermacher, C.C. Petty, and L.W. Owen. Progress towards a predictive model for pedestal height in diii-d. Nuclear Fusion, 49(8):085037, 2009.

[54] V. Genty, T. Rafiq, A. Kritz, and A. Pankin. Predictive modeling of DIII-D tokamak discharges. In Proc. of 54th Annual Meeting of the APS Division of Plasma Physics (Providence, RI, October 29-November 2, 2012), page JP8.00020, 2012.

[55] A.M. Garofalo, X. Gong, C.T. Holcomb, J. Qian, Q. Ren, W.M. Solomon, M. Van Zeeland, B. Wan, G. Xu, O. Meneghini, and G.M. Staebler. Compatibility of internal transport barrier with steady-state operation in the high bootstrap fraction regime on DIII-D. In Proc. of 25th IAEA Fusion Energy Conference (St. Petersburg, Russian Federation 13-18 October 2014), page 657, 2014.

[56] X. Gong, B. Wan, J. Li, and A.M. Garofalo. Development of fully noninductive scenario at high bootstrap current fraction for steady state tokamak operation on DIII-D and EAST. In Proc. of 25th IAEA Fusion Energy Conference (St. Petersburg, Russian Federation 13-18 October 2014), page 215, 2014.

[57] J. Weiland. Stability and Transport in Magnetic Confinement Systems. Springer, 2012.

[58] G. Bateman, A. H. Kritz, A. Y. Pankin, T. Onjun, J. E. McElhenny, and C. MacDonald. Simulations of pedestal formation and ELM cycles. Plasma Physics and Controlled Fusion, 48:A93 – A99, 2006.

[59] Z. Lin, T.S. Hahm, W.W. Lee, W.M. Tang, and R.B. White. Turbulent transport reduction by zonal flows: Massively parallel simulations. Science, 281:1835, 1998.

[60] Z Lin, Y Nishimura, Y Xiao, I Holod, W L Zhang, and L Chen. Global gyrokinetic particle simulations with kinetic electrons. Plasma Physics and Controlled Fusion, 49(12B):B163, 2007.

[61] I. Holod, W.L. Zhang, Y. Xiao, and Z. Lin. Electromagnetic formulation of global gyrokinetic particle simulation in toroidal geometry. Phys. Plasmas, 16:122307, 2009.

[62] B. Adams, W. Bohnhoff, K. Dalbey, J. Eddy, M. Eldred, D. Gay, K. Haskell, P. Hough, and L. Swiler. DAKOTA, a multilevel parallel object-oriented framework for design optimization, parameter estimation, uncertainty quantification, and sensitivity analysis: Version 5.0 user's manual. Tech.Rep. SAND2010-2183, 2010.